JACS
JOURNAL OF THE AMERICAN CHEMICAL SOCIETY
pubs.acs.org/JACS
Article

Elucidating Cathodic Corrosion Mechanisms with Operando Electrochemical Transmission Electron Microscopy

Yao Yang,[‖] Yu-Tsun Shao,[‖] Xinyao Lu, Yan Yang, Hsin-Yu Ko, Robert A. DiStasio, Jr, Francis J. DiSalvo, David A. Muller,* and Héctor D. Abruña*

Cite This: https://doi.org/10.1021/jacs.2c05989
Read Online

ABSTRACT: Cathodic corrosion represents an enigmatic electrochemical process in which metallic electrodes corrode under sufficiently reducing potentials. Although discovered by Fritz Haber in the 19th century, only recently has progress been made in beginning to understand the atomistic mechanisms of corroding bulk electrodes. The creation of nanoparticles as the end-product of the corrosion process suggests an additional length scale of complexity. Here, we studied the dynamic evolution of morphology, composition, and crystallographic structural information of nanocrystal corrosion products by analytical and four-dimensional electrochemical liquid-cell scanning transmission electron microscopy (EC-STEM). Our operando/in situ electron microscopy revealed, in real-time, at the nanometer scale, that cathodic corrosion yields significantly higher levels of structural degradation for heterogeneous nanocrystals than bulk electrodes. In particular, the cathodic corrosion of Au nanocubes on bulk Pt electrodes led to the unexpected formation of thermodynamically immiscible Au−Pt alloy nanoparticles. The highly kinetically driven corrosion process is evidenced by the successive anisotropic transition from stable Pt(111) bulk single-crystal surfaces evolving to energetically less-stable (100) and (110) steps. The motifs identified in this microscopy study of cathodic corrosion of nanocrystals are likely to underlie the structural evolution of nanoscale electrocatalysts during many electrochemical reactions under highly reducing potentials, such as CO_2 and N_2 reduction.

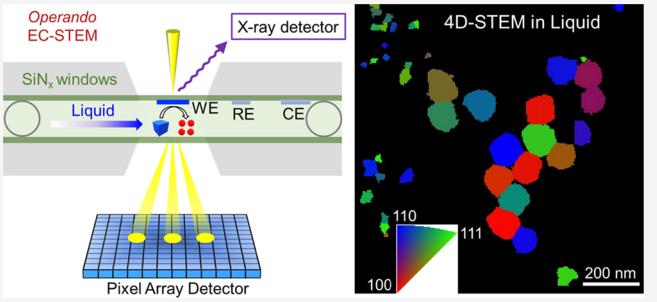

INTRODUCTION

Corrosion is a ubiquitous process in nature and daily life that causes the spontaneous degradation of materials, often metals, by (electro)chemical reactions with their environment.[1] Corrosion processes have a significant economic impact, and it is estimated to cost 3−4% of the gross domestic product of countries.[2−4] Cathodic protection has been widely adapted as an effective strategy to prevent metal corrosion by applying a negative potential or using a sacrificial anode which thermodynamically suppresses the metal oxidation.[1] Conventional wisdom would suggest that metals can stay indefinitely stable in their metallic state under negative potentials. However, it is counterintuitive to observe that corrosion processes emerge again at sufficiently negative potentials, a process that is referred to as *cathodic corrosion*. Originally reported by Fritz Haber in the late 19th century, cathodic corrosion was described as the formation of "metallic dust" from bulk Pt electrodes under cathodic polarization.[5,6] Although cathodic corrosion was briefly studied by Soviet electrochemists in the late 1900s to prepare alloys,[7,8] it remained mostly as empirical observations during the 20th century. Recently, our understanding of cathodic corrosion processes has been revived by the advent of new experimental techniques, especially when applied to Pt single crystals.[9] In 2011, Koper and co-workers reported on the generation of metallic nanoparticles (NPs) by cathodic corrosion with an alternating current (AC).[10,11] Inspired by this pioneering work, extensive efforts have been devoted to examining the effects of different metals, applied potential/current, and electrolyte type and concentration.[12,13] Cathodic corrosion has emerged as a facile surfactant-free top-down method, relative to elaborate colloidal synthesis,[14] to "disintegrate/pulverize" bulk electrodes for NP synthesis of alloys[15−17] and metal oxides,[18] which can be driven by renewable electricity. These electrogenerated catalysts can exhibit enhanced activity and/or selectivity for many renewable energy applications, such as the oxygen reduction/evolution reactions (ORR/OER) for fuel cells,[15] solar-driven water splitting,[18] the reduction of CO_2[16] and nitrite,[11,19,20] and the oxidation of alcohols and NH_3.[10,19]

Despite encouraging progresses, most studies have employed cathodic corrosion of bulk electrodes for NP synthesis, while

Received: June 7, 2022

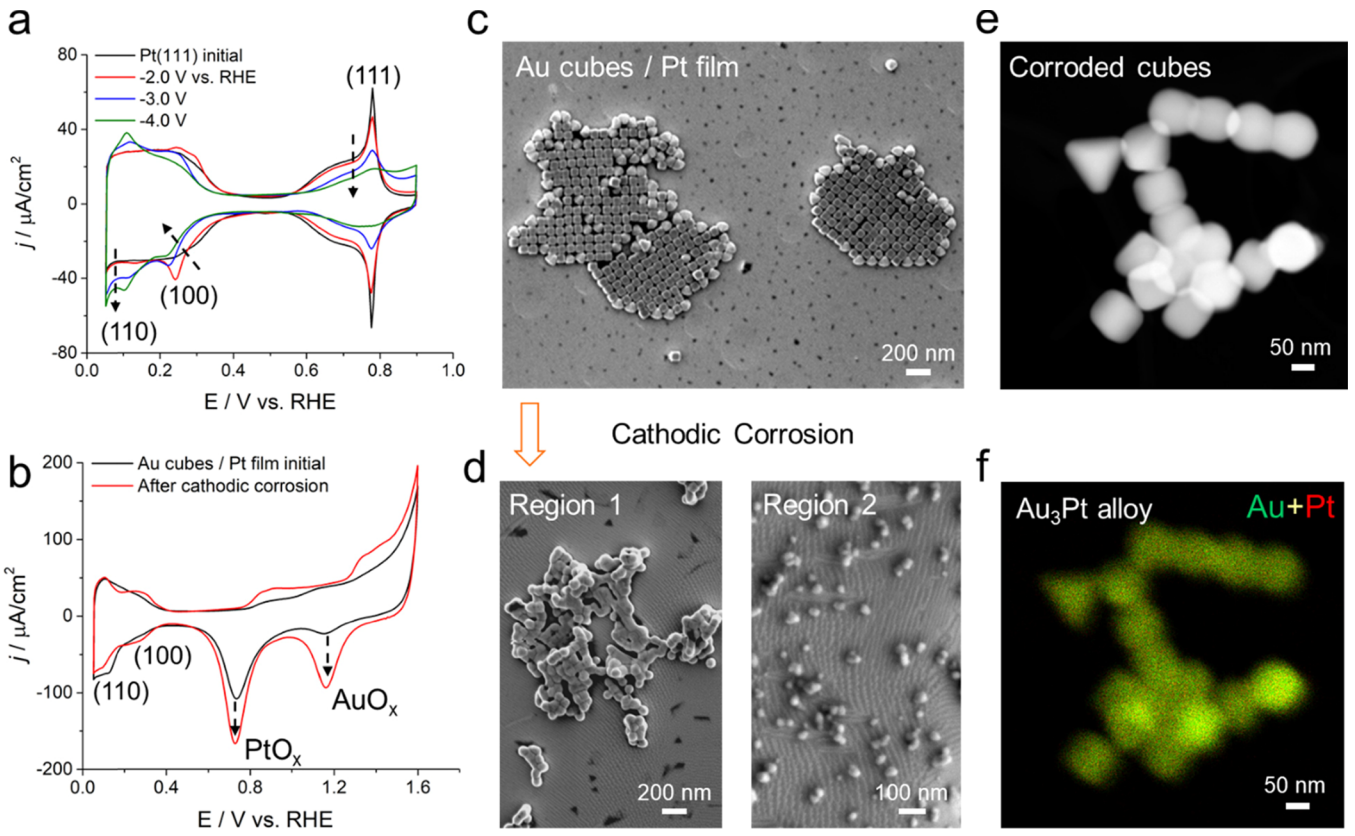

Figure 1. Cathodic corrosion of Pt(111) and Au nanocubes on a poly-Pt electrode. (a) CV profiles of Pt(111) in Ar-sat. 0.1 M $HClO_4$ at 50 mV/s before and after cathodic corrosion. The cathodic corrosion was performed in 0.1 M NaOH at given potentials vs RHE for 2 min. (b) CV profiles of Au nanocubes on a poly-Pt film in Ar-sat. 0.1 M $HClO_4$ at 50 mV/s before and after cathodic corrosion. The cathodic corrosion was performed in 0.05 M $CsClO_4$ at −3 V vs SHE for 30 min. (c) SEM images of pristine Au nanocubes (∼100 nm) on a Pt film. (d) SEM images of Au cubes/Pt film after cathodic corrosion in (b). Region 1 exhibits the formation of deformed/aggregated Au cube clusters and concave pits on the Pt film while Region 2 shows the formation of newly generated smaller NPs (NPs, 20−50 nm) and pronounced stepped etch features on the Pt film. (e and f) STEM-EDX elemental composite maps of Au−Pt alloy NPs with Au in green and Pt in red and an atomic ratio of Au/Pt of 3:1.

few studies have attempted to quantitatively study the cathodic corrosion processes and investigate the reaction mechanisms. Although previous "postmortem" scanning/transmission electron microscopy (S/TEM) studies provide a baseline understanding of the effects of cathodic corrosion,[10−19] they cannot capture real-time changes at electrode−electrolyte interfaces. Furthermore, in contrast to extensive studies of bulk electrodes, the cathodic corrosion of nanocrystals has remained unexplored, due to the lack of operando/in situ microscopy methods. The cathodic corrosion of nanocrystals can provide important insights into structural evolution of nanosized electrocatalysts under reducing potentials, as present in CO_2 and N_2 reduction.[21−26] In addition, the operando methods developed in this study can also advance our understanding of many other electrochemical reactions under strongly reducing or oxidizing potentials, such as the preparation of bulk electrodes with preferential surface orientations with extensive potential cycling to oxidizing potentials[27−29] and shape-controlled metal and metal oxide nanocrystals with large alternating voltage/current methods.[30,31]

The cathodic corrosion processes make it extremely challenging to employ in situ vibrational spectroscopy, operando X-ray methods, or scanning electrochemical microscopy,[32] since the vigorously formed H_2 bubbles can cause severe fluctuations in the spectroscopic or imaging background signals. Although liquid-cell TEM has been widely used to study morphological changes during chemical reactions,[33] only recent studies have shown reliable electrochemical measurements in liquid-cell TEM,[34−37] when compared to standard electrochemical measurements. Conventional EC-TEM employs a liquid thickness of ∼500 nm or above, which hinders/precludes quantitative elemental analysis with energy-dispersive spectroscopy (EDX) or electron energy loss spectroscopy (EELS) as well as crystallographic structural analysis with electron diffraction.[32] There have been several reports on electron diffraction under TEM mode achieved in thin liquids by irradiating the liquid at very high beam doses to form gas bubbles,[38,39] such processes lead to significant changes in pH and compositions of the liquid and thus likely alter the (electro)chemical processes.[32]

Here, we have investigated two model systems, Pt(111) and Au nanocubes on bulk Pt, in an effort to quantitatively characterize cathodic corrosion mechanisms. While Pt(111) showed well-defined anisotropic growth during corrosion, Au nanocubes exhibited significantly higher levels of structural degradation (than bulk Pt) with the formation of Au−Pt alloy NPs. We employed operando/in situ EC-STEM to track dynamics changes in morphology, elemental composition, and crystal structures. In contrast to previous strategies, we took advantage of naturally generated H_2 bubbles, during cathodic corrosion, to form a thin liquid without inducing undesirable beam damage. This enabled STEM imaging, EDX elemental mapping, and 4D scanning electron nanodiffraction (SEND) analysis[40,41] in a native electrolyte environment. With this thin

https://doi.org/10.1021/jacs.2c05989
J. Am. Chem. Soc. XXXX, XXX, XXX−XXX

liquid film strategy, we have been able to carry out, for the first time, a comprehensive investigation of the dynamic structural and compositional evolution of nanocrystals at the nanometer scale, relative to bulk electrodes, during cathodic corrosion. Ex situ atomic-scale STEM imaging and EELS analysis in a H_2-filled gas cell confirmed the structural and compositional information at the same locations as in the in situ measurements. Guided and informed by these microscopic insights, we employed cathodic corrosion as a top-down synthetic method to prepare Au−Pt alloy NPs, which are essentially immiscible, based on their phase diagram. We proposed a cathodic corrosion reaction mechanism involving the formation of Au and Pt hydrides in the presence of adsorbed hydrogen and alkali cations.

RESULTS AND DISCUSSION

Pt single crystals and Au nanocubes on a polycrystalline Pt film were designed as two representative examples of bulk and nanocrystal electrodes to investigate the dynamic structural evolution during cathodic corrosion. Pt single crystals, prepared by the flame annealing technique (Clavilier method),[42] enable a direct correlation between structural changes on atomically flat surfaces and the cathodic corrosion conditions. The cyclic voltammetric (CV) profile of Pt(111) exhibits a well-defined hydrogen region (0.05−0.45 V) and OH ad/desorption regions (0.55−0.9 V), separated by a double-layer region in the middle in 0.1 M $HClO_4$ (Figure 1a, black curve). CV profiles of Pt(100) and Pt(110) exhibit the characteristic hydrogen underpotential deposition (H_{UPD}) peaks at ∼0.3 and ∼0.1 V vs reversible hydrogen electrode (RHE), respectively (Figure S1). Given the flat and featureless plateau of the H_{UPD} of Pt(111), the emergence of any traces of (100) or (110) steps will be evident and unambiguous. The cathodic corrosion of Pt(111) was performed in 0.1 M NaOH at corrosion potentials from −0.5 to −4.0 V vs RHE for 2 min. CV profiles of Pt(111) after corrosion from −0.5 to −1.5 V exhibited negligible changes in the hydrogen region, indicating little or no surface structural changes (Figure S2a). After cathodic corrosion at −2.0 V, the emergence of a pronounced H_{UPD} peak at ∼0.3 V, corresponding to (100) steps, indicated that the onset potential of cathodic corrosion of Pt(111) in 0.1 M NaOH was at around −2.0 V vs RHE (Figure 1a, red curve). At increasingly negative potentials (−3.0 and −4.0 V), the (100) steps gradually diminished, accompanied by the progressive increase of (110) steps at ∼0.1 V (Figure 1a, blue/green curves). The well-defined Pt single crystals enable the accurate and precise quantification of the relative step density by calculating the H_{UPD} charge (Figure S2c and Table S1). The (100) step density exhibited a significant decrease at −3.0 and −4.0 V while the (110) step density exhibited a symmetrical increase (Figure S2c). Interestingly, the overall H_{UPD} charge remained relatively unchanged, indicating a gradual conversion from (100) to (110) steps at more negative corrosion potentials, while the total integrated charge reflected that the total step density remained stable. To rationalize this trend, the H_{UPD} charge values for Pt(111), (100), and (110) were calculated to be 241, 208, and 147 $\mu C/cm^2$ (Figure S1), which are consistent with literature values.[43] The constant H_{UPD} charge values suggest that Pt(111) is the most stable facet with the highest surface atomic density while Pt(110) is the least stable facet with the lowest atomic density. This can explain the trend in anisotropic growth from the most stable Pt(111) to intermediate Pt(100) steps and finally to the most energetically unstable Pt(110) steps, at increasingly negative corrosion potentials. In addition to the changes in the H_{UPD}, the OH_{ads} peak at ∼0.8 V vs RHE in Figure 1a is a characteristic feature of the Pt(111) surface, exhibiting a continuous decay of the OH_{ads} Faradaic charge at increasingly more negative corrosion potentials (Figure S2d and Table S2). This is consistent with the increasing step density revealed from the H_{UPD} measurements and suggests a higher level of surface roughening. SEM images were acquired to visualize the morphological changes during cathodic corrosion. After corrosion at −2.0 V, the Pt(111) electrode changed from a smooth surface to steps and ridges (Figure S3a−d), which, from the CV profiles, corresponds to the formation of (100) steps (Figure 1a). At a very negative corrosion potential of −4.0 V vs RHE, the Pt(111) electrode exhibited sharp stepped features and noticeable concave pits.

The cathodic corrosion of the Pt(111) single crystal was also examined in a nonadsorbing neutral electrolyte, $CsClO_4$ (Figure S4), since it would be suitable for operando/in situ EC-STEM study due to the instability of SiN_x windows in alkaline media. The Pt(111) used above experienced a similar growth of (100) features after corrosion at −2.0 V, and conversion to (110) after corrosion at −3.0 V in $CsClO_4$, although the changes were less pronounced than those in NaOH, which is possibly due to the weaker interaction between Cs^+ and Pt, relative to Na^+.[13] A corrosion onset potential of around −2.0 V vs RHE was found in both 0.05 M $CsClO_4$ and 0.1 M NaOH. A recent study by Koper and co-workers found that the onset potentials of cathodic corrosion of Pt(111) are less negative, at around −0.6 and −0.4 V vs RHE in 1 and 10 M NaOH, respectively, indicating a lower energy barrier for cathodic corrosion at higher hydroxide ion concentrations.[44,45] The cathodic corrosion of Pt single crystals in (Figure 1a) has important implications for tuning electrocatalyst activity. For instance, the ORR activity of Pt(111) in acid was doubled, relative to pristine Pt(111), after cathodic corrosion, which was ascribed to the formation of concave etched features.[44]

The single-crystal Pt(111) study above lays the foundation for investigating the cathodic corrosion of well-defined nanocrystals on a bulk poly-Pt film. Au nanocubes (∼100 nm) with {100}-oriented single-crystal surface facets were selected as an example of inactive electrocatalysts for the hydrogen evolution reaction (HER), in contrast to Pt. The CV profile of pristine Au cubes/Pt film showed a PtO_x reduction peak at ∼0.8 V and a smaller AuO_x reduction peak of the Au nanocubes (Figure 1b). The CV profile after cathodic corrosion in 0.05 M $CsClO_4$ at −3.0 V vs SHE exhibited a 5.4-fold increase in the reduction peak area of AuO_x and a 1.3-fold increase in that of PtO_x (Figure S5a). These changes suggest that Au nanocrystals, with a high surface energy, are subjected to a significantly higher level of structural changes and surface roughening, relative to the bulk Pt electrode. A control experiment of cathodic corrosion of a bulk Au film in $CsClO_4$ under the same conditions exhibited negligible morphological changes based on SEM images, confirming the faster corrosion kinetics of Au nanocrystals than bulk Au counterparts. The H_{UPD} charge revealed a slight increase in Pt(100) steps accompanied by a slight decrease in Pt(110) sites (Figure S5b). Early reports on a poly-Pt wire also showed a similar enrichment of (100) steps after cathodic corrosion.[12,13] SEM images of the Au cubes/Pt film exhibited striking morphological changes after cathodic corrosion

https://doi.org/10.1021/jacs.2c05989
J. Am. Chem. Soc. XXXX, XXX, XXX−XXX

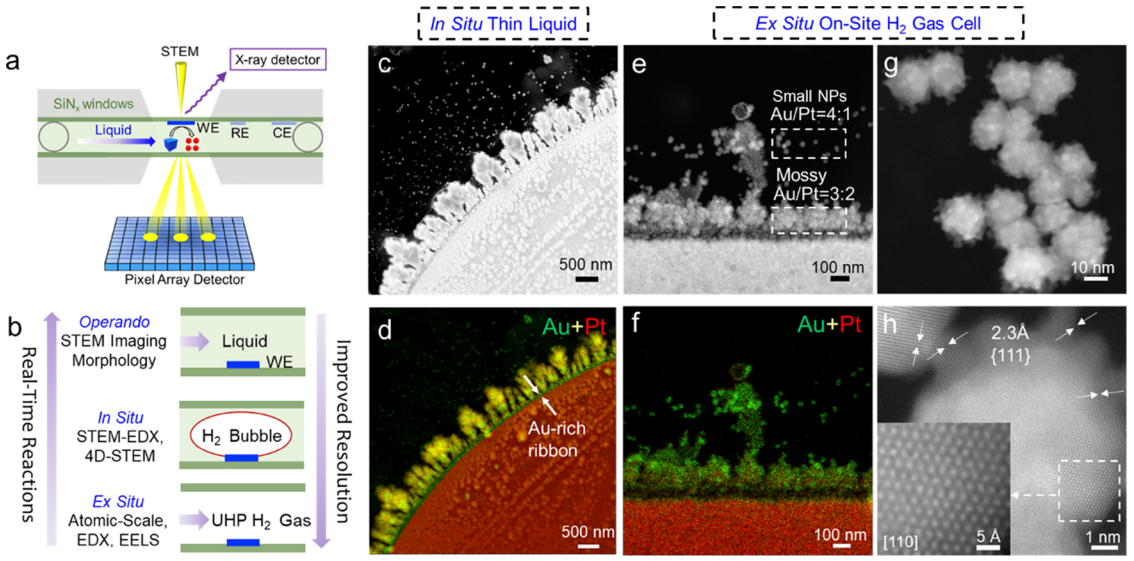

Figure 2. Operando/in situ electrochemical liquid-cell STEM (EC-STEM) studies of cathodic corrosion. (a) Schematic of operando/in situ EC-STEM cell with the capability to enable reliable electrochemical measurements and simultaneously track morphological, compositional, and structural changes under operating conditions. WE, RE, and CE stand for working, reference, and counter electrodes, respectively. SEND based on 4D STEM data sets acquired on an EMPAD. (b) Overview of characterization methodology: Operando EC-STEM for visualizing morphological changes in regular thick electrolyte; in situ EC-STEM for STEM-EDX elemental analysis and SEND for resolving crystal structures. The thin liquid is naturally formed by electrochemically generating a H_2 bubble during cathodic corrosion; ex situ on-site STEM imaging at the atomic scale, in an ultrahigh purity (UHP) H_2 gas cell. (c and d) In situ thin-liquid EC-STEM image and EDX composite maps of Au−Pt alloy nanostructures grown on a Au-rich ribbon (~100 nm) at the bulk Pt electrode after cathodic corrosion of Au cubes on the Pt WE. (e and f) Ex situ high-resolution STEM-EDX, in the H_2 gas cell, showing the coexistence of small Au−Pt alloy NPs (Au/Pt = 4:1) and mossy structures (Au/Pt = 3:2). (g) Ex situ HAADF-STEM image, clearly resolving "nanospikes" at the particle surface. (h) Ex situ atomic-scale lattice image of an Au-rich Au−Pt alloy NP with multiple {111}-oriented domains along different crystal orientations (white arrows). Inset, one Au-alloy domain oriented near the [110] zone axis, magnified from the dashed box.

(Figure 1c,d). Pristine Au nanocrystals exhibited a well-defined cubic morphology and were self-assembled in a periodic pattern/arrangement (Figure 1c). After cathodic corrosion in $CsClO_4$, the Au cubes experienced drastic morphological changes while the bulk Pt electrode showed only mild changes with wrinklelike stepped edges (Figure 1d). Region 1 represents an intermediate state of many cubic particles, which deform and aggregate into clusters, as well as the formation of triangular, square, and rectangular pits on the Pt film, which were suggested to preferentially form on (111), (100), and (110) facets, respectively, based on studies on these low-index Pt single crystals.[45] Region 2 represents a final state of much smaller newly generated, small NPs (10−50 nm) and the coexistence of pronounced stepped etching features on the Pt film (Figures 1d and S6). STEM-EDX elemental maps of corroded Au nanocubes and newly generated NPs (~20 nm) showed homogenous elemental distributions of Au and Pt, indicating the formation of single-phase Au_3Pt alloy NPs (Figures 1e,f and S7). In summary, during cathodic corrosion, Pt films and Au nanocubes were "atomized" so that highly mobile Pt atoms were injected into the Au cubes to form Au−Pt alloy NPs. It is possible that the disintegration of bulk Pt and the deformation/aggregation of Au nanocubes occur simultaneously and are strongly modulated by the local electrical field, interfacial pH, and concentration of alkali cations. Although it is challenging to quantify the corrosion rate, nanocrystals experienced a significantly higher level of structural destruction than the bulk electrodes.

To elucidate the structural and elemental evolution of nanocrystals and bulk electrodes, we employed operando/in situ EC-STEM, including STEM imaging, EDX elemental mapping, and SEND diffraction imaging. Figure 2a presents a cross section of the operando/in situ EC-STEM cell with a three-electrode configuration, including working, reference, and counter electrodes (WE, RE, and CE). The SEND works by using an electron microscope pixel array detector (EMPAD) to record the 2D electron diffraction pattern over a 2D grid of probe positions, resulting in 4D data sets,[46] which can dramatically reduce beam dose while retrieving temporal and spatially resolved structural information in liquids. We designed an experimental strategy to enable operando, in situ and ex situ EC-STEM operation in the same cell, and at identical locations to enable reliable electrochemical measurements and simultaneously probe real-time interfacial changes across multiple length scales, by generating H_2 bubbles to reversibly control the liquid thickness (Figure 2b). Operando EC-STEM was employed to track the morphological changes under similar reaction conditions to standard electrochemical measurements in Figure 1a,b but was not able to perform EDX nor SEND analysis in thick electrolytes. The thin liquid, naturally formed by H_2 bubbles during cathodic corrosion, dramatically improved spatial resolution and enabled nanometer scale in situ STEM-EDX and SEND in a native electrolyte, which nonetheless, deviates from optimal electrochemical conditions. To resolve atomic-scale lattice structures, H_2 gas was flowed to completely remove the liquid while preserving the corroded electrode in a reducing environment. Ex situ EC-STEM, despite the lack of real-time information, serves as an identical-location STEM to perform on-site characterization before and after cathodic corrosion. Ex situ STEM also improves the spatial resolution of EDX and EELS

https://doi.org/10.1021/jacs.2c05989
J. Am. Chem. Soc. XXXX, XXX, XXX−XXX

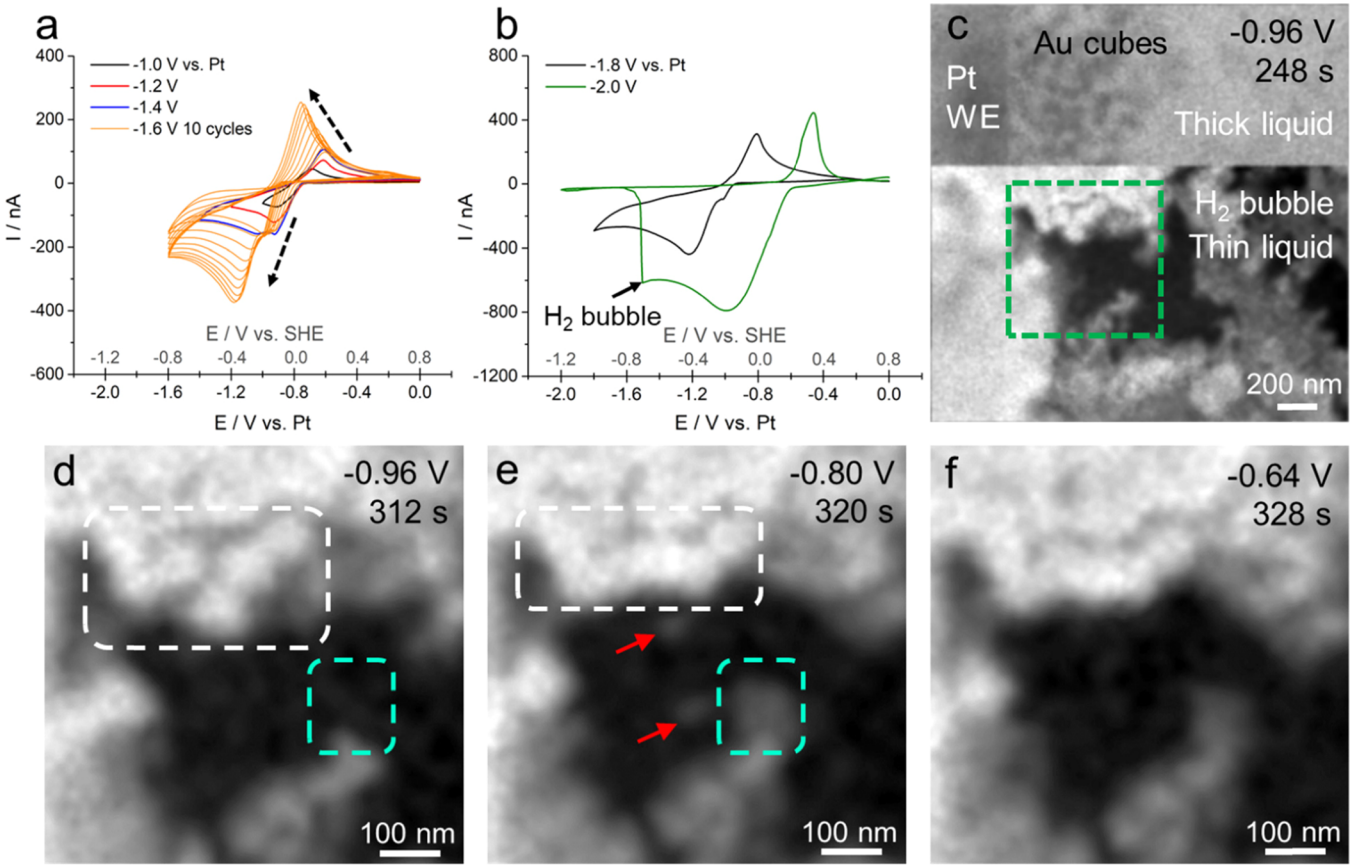

Figure 3. Operando EC-STEM studies of dynamic morphological changes during cathodic corrosion. (a) CV profiles of Au cubes on Pt WE in 1 mM $CsClO_4$ in EC-STEM in a regular thick electrolyte with various lower potential limits from −1 to 1.6 V vs Pt at 100 mV/s. Ten continuous cycles from −1.6 to 0 V (orange profiles) are shown to demonstrate the process of accumulating soluble H_2 and other reaction intermediates. The potential of the Pt pseudo RE was determined to be around 0.8 V vs SHE based on standard electrochemical measurements in Figure S9. (b) CV profiles with lower limits at −1.8 and −2.0 V vs Pt. At −2.0 V, the H_2 concentration in the electrolyte reaches saturation and generates a H_2 bubble, which caused a sharp current drop to nearly zero. (c) Representative example of the dramatically enhanced spatial resolution enabled by the formation of H_2 bubble. (d–f) Three continuous STEM imaging frames from the orange box in (c) showing the dynamic morphological changes during cathodic corrosion. The dashed white boxes mark the reconstruction of two large NP clusters into a longer particle chain. The red arrows point the migration of two clusters of small NPs and the green boxes mark the growth of new NPs.

elemental analysis by circumventing the undesirable beam damage and sample drift in liquids.

In an effort to demonstrate that operando EC-STEM is capable of delivering reliable electrochemical measurements, we performed CV measurements of Pt in acid and Cu electrodeposition (Figure S9). CV profiles of Pt in acid in the EC-STEM cell matched well the standard electrochemical measurements of Pt in Figure 1a and showed no evidence of beam damage at a dose of ~300 e/nm^2. The potential of the Pt pseudo-RE was estimated to be about +0.8 V vs SHE based on the H_{UPD} peak position of Pt. CV profiles in $CuSO_4$ showed the well-defined Cu electrodeposition and stripping peaks at around −0.65 V vs Pt, which is consistent with the potential (−0.648 V) at which the largest amount of deposited Cu nanoclusters occurred (Figure S9). The onset potential of Cu electrodeposition was estimated to be 0.25 V vs SHE in the operando EC-STEM study, which matches well with the theoretical value of E^0 (Cu^{2+}/Cu) in 10 mM $CuSO_4$ (0.22 V vs SHE). With a rigorous electrochemical protocol established, we performed operando EC-STEM studies of cathodic corrosion of Au nanocrystals on a bulk Pt electrode. The cathodic corrosion was first performed on a bare Pt WE as a control study (Figure S10). After applying sufficiently negative potentials (−1.5 V vs Pt), noticeable mossy features appeared on the bulk Pt electrode surface, while no mossy features were evident in the absence of alkali cations, indicating the important role of alkali cations to initiate cathodic corrosion. Operando EC-STEM was then employed to investigate the cathodic corrosion of Au nanocubes on bulk Pt working electrodes (Au cubes/Pt WE) in 1 mM $CsClO_4$. CV profiles of Au cubes/Pt WE exhibited the characteristic oxidation peaks of both Au and Pt at ~0.6 V vs Pt (~1.4 V vs SHE) (Figure S11), which matched the standard electrochemical measurements in Figure 1b. To explore the effects of corrosion potentials, the lower potential limit was systematically lowered from −1.0 to −2.0 V (Figure 3a,b). As the lower potential limit was lowered from −1.0 to −1.6 V, the peak current density of the redox couple gradually increased (Figure 3a). Ten continuous CV cycles from 0 to −1.6 V vs Pt at 100 mV/s are plotted as an example, to show the progressive growth of well-defined redox couples with shoulder peaks at −1.0 V vs Pt. When the lower potential limit was further decreased to more negative values of −1.8 and −2.0 V, a rapid current drop to nearly zero was observed at around −1.5 V vs Pt, corresponding to the formation of H_2 bubbles, which created a native thinner liquid layer (Figure 3b). The gradual increase of peak currents at

https://doi.org/10.1021/jacs.2c05989
J. Am. Chem. Soc. XXXX, XXX, XXX−XXX

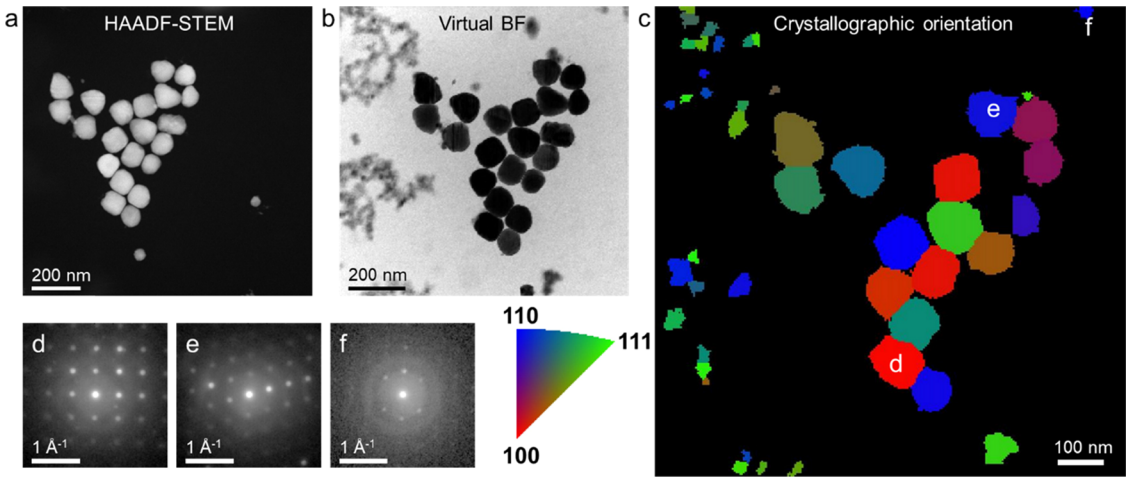

Figure 4. In situ SEND of reacted Au nanocubes and Au−Pt NPs in thin liquid. (a) HAADF-STEM image of reacted Au nanocubes near the Pt WE in a thin layer of 1 mM $CsClO_4$. SEND, based on a 4D data set, was acquired by recording a 2D diffraction pattern at each probe position in a 2D grid. (b) Virtual BF image reconstructed from the SEND data set, showing larger Au cubes (∼100 nm) and smaller Au−Pt NPs (20−50 nm). (c) Crystallographic orientation map obtained by careful indexing of each clustered diffraction pattern using an fcc structure model. (d−f) Representative diffraction patterns shown in the logarithmic scale from labeled regions in (c), respectively.

more negative potentials and during continuous CV cycles is possibly due to the accumulation of higher concentrations of soluble H_2 and other reaction intermediates during cathodic corrosion in the presence of alkali cations. Once the H_2 concentration in the electrolyte reaches a critical saturation concentration, a H_2 bubble forms instantaneously. A recent study by White and co-workers reported that H_2 bubble nucleation on Pt nanoelectrodes follow first-order kinetics and the nucleation rate can increase by four orders of magnitude over a very small relative change in the H_2 concentration at the electrode surface.[47] The possibility of diffusion of Pt ions from Pt CE to WE was excluded given the large distance between CE and WE (Figure S12). The current density in operando EC-STEM in Figure 3a,b is of the order of ∼20 mA/cm^2 in $CsClO_4$ solution, which is comparable to the value of ∼10 mA/cm^2 under similar cathodic corrosion conditions in a standard electrochemical cell (Figures S12 and S13).

Operando EC-STEM imaging was employed to track the morphological changes during cathodic corrosion. Operando EC-STEM images showed little morphological changes during the first 200 s cycling between 0 and −1.6 V vs Pt at 20 mV/s (Figure S14a,b). After 248 s, a H_2 bubble emerged and pushed away the electrolyte, leading to a dramatically improved spatial resolution (Figures 3c and S15). The upper part of the STEM image in Figure 3c illustrates that the Au nanocubes are barely visible in the thick liquid film. Once a H_2 bubble is electrochemically generated, the STEM image of the NPs can be clearly resolved. Operando EC-STEM images in Figure 3d−f exhibit the dynamic morphological changes during cathodic corrosion over three continuous frames magnified from the orange box in Figure 3c. Two large NP clusters of 100−200 nm experienced particle agglomeration into one longer particle chain (white dashed boxes in Figure 3d,e). In addition, two small new particles of ∼30 nm emerged and migrated in between these large particle clusters (red arrows, Figure 3e). Individual particle growth was also observed (green boxes in Figure 3d,e). These particle reconstruction/migration/growths were obtained at a very low beam dose of ∼8 e/nm^2, which was caused by cathodic corrosion, rather than beam-induced artifacts, as verified by a beam dose control experiment at a higher dose of 15 e/nm^2 over longer-time STEM imaging (Movie S1). The full details of the morphological changes and image processing for Figure 3d can be found in Movie S2 and Figure S15. A static STEM image in Figure S16 exhibited the coexistence of partially reacted Au cubes (∼100 nm) and newly generated small NPs (20−50 nm) at the solid−liquid−gas interface, quantitatively reproducing the formation of small alloy NPs in Figure 1d.

In situ EC-STEM in thin liquid films, enabled carrying out STEM-EDX elemental analysis in an electrolyte (Figure 2c,d). After pushing away most of the bulk electrolyte, newly grown nanostructures were clearly observed at the Pt electrode surface (Figure 2c). In situ STEM-EDX composite elemental mapping at a dose of ∼8500 e/nm^2 exhibited a striking inhomogeneous elemental distribution of Au and Pt where Au−Pt alloy nanostructures were grown on a Au-rich ribbon (∼100 nm, green) on the bulk Pt electrode (red) (Figure 2d). The drastic changes from Au nanocubes to Au−Pt alloy nanostructures suggest a much higher level of structural degradation for nanocrystals during corrosion, relative to the mild changes exhibited by the bulk electrodes. Quantification of STEM-EDX spectra yielded a Au/Pt atomic ratio of ∼1:1 for these alloy nanostructures, and ∼ 5:1 for newly formed Au-rich alloy NPs (∼30 nm) located in the upper left corner (Figure S17). The presence of a thin liquid film was indicated by the significantly higher intensity of O signals in EDX (Figure S17) as well as the rapid flow of NPs as shown in Movie S3. Minimal beam damage was observed after EDX mapping (Figure S18).

In addition to morphological and elemental information obtained by in situ EC-STEM, crystallographic structural information was derived from 4D STEM data sets by performing in situ SEND in the thin liquid film (Figure 4). For example, Figure 4a shows a high-angle annular dark-field (HAADF) image of reacted Au nanocubes and newly generated Au−Pt alloy NPs. A virtual bright-field (BF) image (Figure 4b) was reconstructed from the SEND data set by integrating the transmitted (000) spot, which revealed additional mossy particles of 20−50 nm in the left region of the image. The crystallographic orientation of each NP was

https://doi.org/10.1021/jacs.2c05989
J. Am. Chem. Soc. XXXX, XXX, XXX−XXX

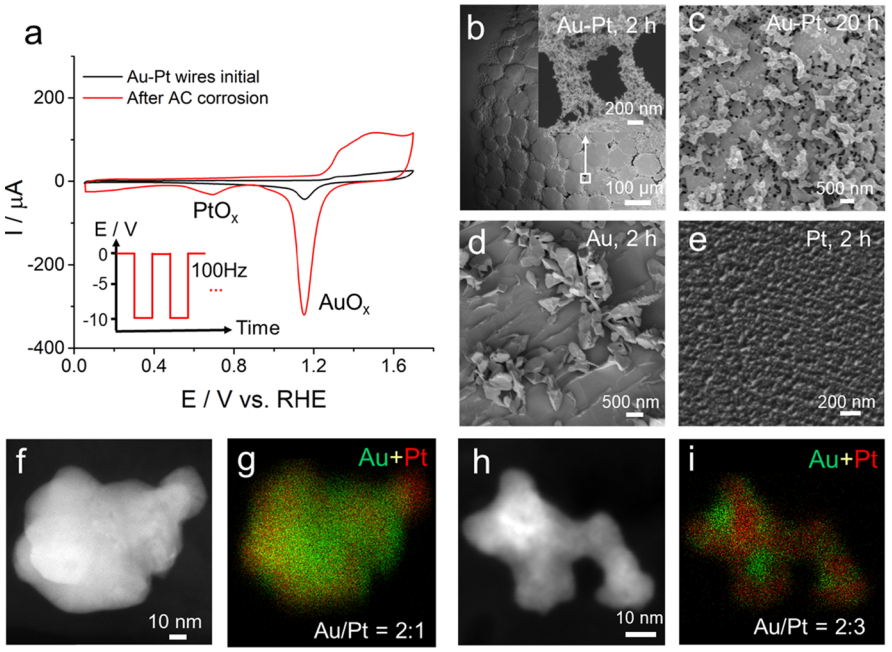

Figure 5. Cathodic corrosion for the synthesis of Au−Pt bimetallic NPs. (a) CV profiles of Au−Pt mixed wires in Ar-sat. 0.1 M $HClO_4$ at 50 mV/s before and after cathodic corrosion in 10 M KOH for 2 h. The inset shows the corrosion conditions with an AC square wave between 0 and −10 V with a DC offset at −5 V at a frequency of 100 Hz. (b) SEM images of Au−Pt wires after corrosion for 2 h showing the cracking of bulk electrodes and generation of numerous small NPs. (c) SEM image of Au−Pt wires after corrosion for 20 h showing a much higher level of surface roughening, relative to 2 h in (b). (d and e) SEM images of a Au wire (d) and Pt wire (e) under the same cathodic corrosion conditions after 2 h. (f−i) STEM images and EDX elemental maps of newly generated Au−Pt bimetallic particles from Au−Pt wires after cathodic corrosion processes in (a).

retrieved by indexing the diffraction patterns for each cluster using an fcc structure model. Figure 4c shows the reconstructed crystallographic orientation map, where the color represents the superposition of three corners ({100}, {110}, and {111} as R, G, and B, respectively) in the inverse pole figure. Figure 4d−f shows representative diffraction patterns from labeled regions in Figure 4c with orientations near the zone axes of [100], [110], and [110], respectively. The left region in Figure 4c exhibits the crystal orientation of highly polycrystalline mossy structures. The thickness of the thin liquid film was estimated to be around 100 nm (Figure S19), using the EELS plasmon peak and the zero-loss peak.[48] This indicates that a 50 nm liquid film is covering each SiN_x window, which is comparable to the estimation in a similar liquid-cell configuration in a recent EELS study by Stach and co-workers.[49] In the future, we plan to employ molecular dynamics (MD) simulations (in conjunction with the SEND analysis) as an alternative approach to quantify the liquid film thickness in the vicinity of the amorphous SiN_x window (see Supporting Information). In addition, SEND illustrates the polycrystalline nature of the newly generated Au−Pt alloys (Figure S20) after corroding the Au nanocubes on the Pt film in Figure 1d, which serves as a valuable complementary structural information for STEM-EDX maps in Figure S8b. This is the first demonstration that in situ SEND diffraction analysis, in thin liquids, serves as a powerful tool to provide structural insights beyond morphological and compositional changes.

Ex situ EC-STEM in the H_2 gas cell was employed to resolve the atomic lattice structure of individual alloy NPs (Figure 2e−h). A significant improvement of the spatial resolution was demonstrated in the H_2 gas cell by resolving the subtle features of Au−Pt NPs and mossy structures (Figure 2e), which were not accessible in the thin liquid film images (Figure S21). STEM-EDX in the H_2 gas cell showed that, in general, the small NPs were Au-rich alloys with Au/Pt atomic ratios of 4∼5:1, while the mossy structures near the Pt WE had Au/Pt atomic ratios of 1.5∼1:1 (Figures 2e,f and S22−S24). Figure S24 presents an example of a Au nanocube that was in the process of being converted into mossy structures and small alloy NPs by the Pt WE. The above STEM-EDX analysis has provided unique insights into the locally heterogenous elemental distributions of Au−Pt alloys after cathodic corrosion. It should be noted that the Ti peaks in the EDX spectra (Figures S17 and S22−24) are from the Ti adhesion layer under the Pt WE. Ex situ STEM-EELS in the H_2 gas cell showed the presence of Au and Pt and the absence of Ti, confirming that the alloy NPs contained only Au and Pt (Figure S25). The absence of Cs also rules out the formation of Cs-intercalation compounds after corrosion. Valence EELS, based on the relative intensity of the plasma peak,[48] allowed estimating the thickness of Au−Pt alloy NPs and corroded Pt WE as 50 and 100 nm, respectively (Figure S26). Ex situ EC-STEM also enabled the direct visualization of crystal structures at the atomic scale (Figure 2g,h). Small Au−Pt alloy NPs exhibited "nanospikes" on the particle surface (Figure 2g), which are not readily visible in the thin liquid film (Figure S21). An atomic-scale HAADF-STEM image exhibited the polycrystalline nature of the small alloy NPs (Figure 2h). Given the Au-rich composition of the small alloy NPs and the close values of lattice parameters (a_{Au} = 4.078 Å, a_{Pt} = 3.923 Å), it is reasonable to use the *d*-spacing values of pure Au to index the lattice images of these Au_5Pt alloy NPs (Figure S27). Multiple {111}-oriented domains of a few nanometer were visualized along different crystal orientations. The domain magnified from the dashed box in Figure 2h exhibited an fcc

https://doi.org/10.1021/jacs.2c05989
J. Am. Chem. Soc. XXXX, XXX, XXX−XXX

lattice domain oriented near the [110] zone axis. Atomic-scale STEM images of other Au−Pt alloy NPs and mossy structures confirmed their polycrystalline nature (Figures S27−28).

Cathodic corrosion can serve as an effective top-down synthetic method to "disintegrate" bulk electrodes into alloy NPs. Au and Pt intertwined wires were subjected to cathodic corrosion in 10 M KOH with an AC square wave (−10 ∼ 0 V) at 100 Hz with a direct current (DC) offset of −5 V to ensure a reduction process (Figure 5a, inset). After corrosion for 2 h, the CV profiles of the Au−Pt wires exhibited a fivefold increase of the AuO_x reduction peak and an evident PtO_x reduction peak, relative to pristine electrodes (Figure 5a). After cathodic corrosion, the CV profiles of the Au−Pt wires exhibited the H_{UPD} features of polycrystalline Pt, indicating that Au was subjected to a higher level of corrosion relative to Pt (Figure S29). SEM images of Au−Pt wires after 2 h of corrosion indicated that the electrode had cracked into micrometer-sized domains generating new NP clusters of 10−100 nm (Figures 5b and S30). After a longer corrosion time of 20 h, the Au−Pt wires further disintegrated into a highly porous surface (Figures 5c and S30c,d). In order to deconvolute the morphological changes of Au from Pt, cathodic corrosion of individual Au and Pt wires were performed under the same conditions. SEM images of the Au wire after corrosion, exhibited the formation of needle-shaped nanocrystals and noticeable etching steps on the electrode surface (Figure 5d), which corresponded to a 10-fold increase of the AuO_x reduction peak (Figure S31a). In comparison, SEM images of Pt showed much milder etching features (Figure 5e) and only an ∼15% increase of the ECSA (Figure S31b). Such differences between Au and Pt can be rationalized by the competition between cathodic corrosion and their HER activities. The HER kinetics on Au are so sluggish that the strongly reducing potentials mainly drive the corrosion of the bulk Au into nanocrystals. In contrast, the HER occurs readily on Pt below 0 V vs RHE, which makes the very negative potentials primarily drive the HER while causing milder morphological changes as a result of the corrosion. STEM-EDX maps of the as-synthesized NPs showed the elemental distribution of Au−Pt alloy NPs with multiple Au-rich (green) and Pt-rich (red) domains of a few nanometer (Figure 5) with average Au/Pt ratios ranging from 2:1 to 2:3 (Figure S32). The disintegration of Au and Pt bulk wires into Au−Pt bimetallic NPs yielded a certain level of alloying at the nanometer scale but not a single phase as that formed by corrosion of the Au nanocubes on the Pt film (Figure 1e,f). This is ascribed to the significantly higher corrosion rate of nanocrystals, relative to bulk electrodes in Figure 5. Thus, cathodic corrosion shows the potential to overcome the thermodynamic solubility limitations of phase diagrams and enable the incorporation of Au into Pt lattices, which has been reported to enhance durability of platinum group metal (PGM)-based ORR electrocatalysts.[50,51] Cathodic corrosion of other largely immiscible alloys from bulk electrodes, such as Pt−M (M = Bi, Pb, and Pr),[15,17] Au−Co,[11] and Sn−Pb[16] also show noticeable evidence of phase and/or elemental segregation of the synthesized alloy NPs. By optimizing cathodic corrosion conditions and environments, cathodic corrosion has the potential to enable preparation of single-phase alloys with tunable structures and compositions.

Although the exact cathodic corrosion mechanisms are still under investigation, based on this study and Koper's previous work,[9] we propose the following possible reaction pathways for the cathodic corrosion of Au nanocubes on bulk Pt electrodes (Figure 6). At sufficiently negative potentials, atomic hydrogen

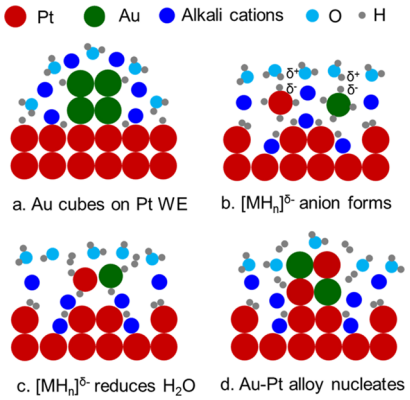

Figure 6. Schematic of the proposed cathodic corrosion mechanisms. (a) Cathodic corrosion is initiated by the presence of atomic hydrogen and adsorbed alkali cations at sufficiently negative potentials. (b) Pt and Au atoms are electrochemically converted to metal hydrides (e.g., $[MH_n]^{\delta-}$), which are stabilized by alkali cations when in close proximity. (c) Highly reducing, negatively charged hydrogen (ostensibly hydride) in $[MH_n]^{\delta-}$ anions reacts with water, resulting in an extremely short-lifetime intermediate species. (d) Au and Pt atoms encounter and nucleate in the form of Au−Pt bimetal alloys, leading to the growth of alloy NPs. Note: Only one Au and one Pt atom in (b and c) were drawn for the purpose of simplification.

is generated, in the presence of alkali cations (Na^+, K^+, and Cs^+), which adsorbs on the Au and Pt surfaces (Figure 6a). Adsorbed hydrogen (H*) and alkali cations can induce a surface reconstruction and initiate the corrosion from flat terraces to roughened step edges. Au nanocubes, with a larger surface energy, are subjected to faster corrosion kinetics, relative to bulk Pt. Mobile Au and Pt atoms, etched from electrode surfaces, are hypothesized to form metal hydrides and diffuse to nearby electrolyte (Figure 6b), potentially contributing to the redox peaks in Figure 3a,b. A general chemical formula of metal hydrides can be written as $[MH_n]^{\delta-}$,[13] such as $[AuH_2]^-$, $[AuH_4]^-$, and $[PtH_4]^{2-}$, depending on the valence states of the metal centers (M = Pt or Au). For simplicity, $[MH_4]$ with four hydrogen atoms was used to represent metal hydride anions in the mechanistic illustration in Figure 6. These metal hydride anionic species, while unconfirmed, can be stabilized by alkali cations in a locally strong reducing environment. When metal hydrides encounter water molecules at appropriate collision orientations, the negatively charged H in $[MH_n]^{\delta-}$ reacts instantaneously with the positively charged H in H_2O (Figure 6b) and results in the formation of elemental Au and Pt atoms (Figure 6c). Thus, these metal hydrides, once generated, have extremely short lifetimes and are very challenging to isolate and analyze. These newly generated Au and Pt atoms nucleate and grow into Au−Pt alloy NPs (Figure 6d). At reducing potentials well below equilibrium, the cathodic corrosion process leads to the formation of highly active Au−Pt bimetallic anions and subsequent quenching and deposition of Au−Pt alloy NPs, which can achieve metastable phases that are normally immiscible in the phase diagram (Figure S33). The proposed Pt hydrides, such as $Na_2[PtH_4]$ and $Cs_2[PtH_4]$, have been previously synthesized with Pt and alkali hydrides.[52] The presence of Au hydrides has been experimentally confirmed at ultralow temperatures.[53] A recent study by

https://doi.org/10.1021/jacs.2c05989
J. Am. Chem. Soc. XXXX, XXX, XXX−XXX

Hoffmann and co-workers predicted that ternary Au hydrides could be thermodynamically stabilized by alkali cations under ambient conditions.[54] In addition, the presence of surface gold hydride on nanostructured gold catalysts was evidenced by inelastic neutron scattering.[55] Alkali cations are required to induce the cathodic corrosion since the corrosion process does not occur if the protons are the only cations in solution.[13] In summary, the current hypothesis, pending experimental verification, suggests that cathodic corrosion mechanisms likely involve key intermediates, such as ternary metal hydrides, in the presence of alkali cations. We anticipate that additional theoretical calculations and operando/in situ vibrational spectroscopy will contribute to the identification of key reaction intermediates, metal hydrides, in the proposed mechanism and advance our understanding of this highly kinetically driven corrosion process.

CONCLUSIONS

In conclusion, this work reports on the anisotropic cathodic corrosion processes of Pt single crystals and reveals, for the first time, the dynamic corrosion process of nanocrystals, which have significantly faster corrosion kinetics than bulk electrodes. Operando/in situ EC-STEM in regular electrolyte and thin liquid filmss, as well as ex situ STEM in a H_2 gas cell, has enabled the direct probing of morphological, compositional, and structural changes at nanometer and atomic scales. Guided by microscopic insights from operando EC-STEM, we demonstrate that cathodic corrosion can serve as a top-down surfactant-free alloy NP synthesis method, which can overcome the thermodynamic limitations of phase diagrams. Cathodic corrosion of nanocrystals can provide valuable insights into the structural evolution of widely used nanosized electrocatalysts under reducing potentials, such as in CO_2 and N_2 reduction. Such unintentional structural changes of nanosized electrocatalysts occurring within the potential window of cathodic corrosion can have a great impact on electrocatalyst activity/selectivity and electrode stability. This study provides valuable insights to utilize cathodic corrosion to tailor the structures and compositions of nanosized electrocatalysts for enhanced activity and selectivity. A microscopic understanding of the cathodic corrosion of nanocrystals will help circumvent the undesirable corrosion under reducing potentials, so as to develop corrosion-resistant electrocatalysts. Operando EC-STEM offers a platform for advancing the microscopic understanding of cathodic corrosion, which can be extended to the study of other renewable energy-related electrochemical reaction mechanisms at electrode−electrolyte interfaces under realistic operating conditions.

ASSOCIATED CONTENT

Supporting Information

The Supporting Information is available free of charge at https://pubs.acs.org/doi/10.1021/jacs.2c05989.

Beam dose control experiments at a dose of 15 e/nm^2 (Movie S1), dynamic cathodic corrosion process of Au cubes on the Pt WE in EC-STEM (Movie S2), and rapid flow of NPs in the thin liquid layer (Movie S3) (ZIP)

Experimental Section (Materials and Methods), Figures S1−S33, Tables S1 and S2, and References 56−63 (PDF)

AUTHOR INFORMATION

Corresponding Authors

David A. Muller − *School of Applied and Engineering Physics and Kavli Institute at Cornell for Nanoscale Science, Cornell University, Ithaca, New York 14853, United States;* orcid.org/0000-0003-4129-0473; Email: dm24@cornell.edu

Héctor D. Abruña − *Department of Chemistry and Chemical Biology, Cornell University, Ithaca, New York 14853, United States;* orcid.org/0000-0002-3948-356X; Email: hda1@cornell.edu

Authors

Yao Yang − *Department of Chemistry and Chemical Biology, Cornell University, Ithaca, New York 14853, United States;* orcid.org/0000-0003-0321-3792

Yu-Tsun Shao − *School of Applied and Engineering Physics, Cornell University, Ithaca, New York 14853, United States*

Xinyao Lu − *Department of Chemistry and Chemical Biology, Cornell University, Ithaca, New York 14853, United States;* orcid.org/0000-0002-2649-5721

Yan Yang − *Department of Chemistry and Chemical Biology, Cornell University, Ithaca, New York 14853, United States*

Hsin-Yu Ko − *Department of Chemistry and Chemical Biology, Cornell University, Ithaca, New York 14853, United States;* orcid.org/0000-0003-1619-6514

Robert A. DiStasio, Jr − *Department of Chemistry and Chemical Biology, Cornell University, Ithaca, New York 14853, United States;* orcid.org/0000-0003-2732-194X

Francis J. DiSalvo − *Department of Chemistry and Chemical Biology, Cornell University, Ithaca, New York 14853, United States*

Complete contact information is available at: https://pubs.acs.org/10.1021/jacs.2c05989

Author Contributions

[‖]Y.Y. and Y.-T.S. contributed equally to this work

Funding

This work was primarily supported by the Center for Alkaline-Based Energy Solutions (CABES), an Energy Frontier Research Center (EFRC) program supported by the U.S. Department of Energy, under grant DE-SC0019445. This work made use of TEM facilities at the Cornell Center for Materials Research (CCMR) which are supported through the National Science Foundation Materials Research Science and Engineering Center (NSF MRSEC) program (DMR-1719875). The paper is partially adapted from the PhD Thesis by Y. Y. (Cornell University 2021).

Notes

The authors declare no competing financial interest.

REFERENCES

(1) von Baeckmann, W.; Schwenk, W.; Prinz, W. *Handbook of Cathodic Corrosion Protection*; Elsevier: Amsterdam, 3rd ed., 1997.

(2) Koch, G. H.; Brongers, M. P. H.; Thompson, N. G.; Virmani, Y. P.; Payer, J. H. *Corrosion Costs and Preventive Strategies in the United States*. Federal Highway Administration (FHWA), 2002, FHWA-RD-01-156.

(3) Biezma, M. V.; Schanack, F. Collapse of Steel Bridges. *J. Perform. Constr. Facil.* **2007**, *21*, 398−405.

(4) Cole, I. S.; Marney, D. The Science of Pipe Corrosion: A Review of The Literature on The Corrosion of Ferrous Metals In Soils. *Corros. Sci.* **2012**, *56*, 5−16.

(5) Haber, F. Über Elektrolyse der Salisbury Nebst Mitteilungen Über Kathodische Formation von Blei. *Z. Anorg. Chem.* **1898**, *16*, 438−449.
(6) Haber, F. The Phenomenon of The Formation of Metallic Dust From Cathodes. *Trans. Am. Electrochem. Soc.* **1902**, *2*, 189−196.
(7) Kabanov, B. N.; Astakhov, I. I.; Kiseleva, I. G. Formation of Crystalline Intermetallic Compounds and Solid Solutions in Electrochemical Incorporation of Metals into Cathodes. *Electrochim. Acta* **1979**, *24*, 167−171.
(8) Salzberg, H. W.; Mies, F. Cathodic Disintegration of Tin. *J. Electrochem. Soc.* **1958**, *105*, 64−66.
(9) Hersbach, T. J. P.; Koper, M. T. M. Cathodic Corrosion: 21st Century Insights into A 19th Century Phenomenon. *Curr. Opin. Electrochem.* **2021**, *26*, No. 100653.
(10) Yanson, A. I.; Rodriguez, P.; Garcia-Araez, N.; Mom, R. V.; Tichelaar, F. D.; Koper, M. T. M. Cathodic Corrosion: A Quick, Clean, and Versatile Method for the Synthesis of Metallic NPs. *Angew. Chem., Int. Ed.* **2011**, *50*, 6346−6350.
(11) Rodriguez, P.; Tichelaar, F. D.; Koper, M. T. M.; Yanson, A. I. Cathodic Corrosion as a Facile and Effective Method to Prepare Clean Metal Alloy NPs. *J. Am. Chem. Soc.* **2011**, *133*, 17626−17629.
(12) Hersbach, T. J. P.; Yanson, A. I.; Koper, M. T. M. Anisotropic Etching of Platinum Electrodes at the Onset Of Cathodic Corrosion. *Nat. Commun.* **2016**, *7*, 12653.
(13) Hersbach, T. J. P.; McCrum, I. T.; Anastasiadou, D.; Wever, R.; Calle-Vallejo, F.; Koper, M. T. M. Alkali Metal Cation Effects in Structuring Pt, Rh, and Au Surfaces through Cathodic Corrosion. *ACS Appl. Mater. Interfaces* **2018**, *10*, 39363−39379.
(14) Xia, Y.; Xia, X.; Peng, H.-C. Shape-Controlled Synthesis of Colloidal Metal Nanocrystals: Thermodynamic versus Kinetic Products. *J. Am. Chem. Soc.* **2015**, *137*, 7947−7966.
(15) Fichtner, J.; Garlyyev, B.; Watzele, S.; El-Sayed, H. A.; Schwämmlein, J. N.; Li, W.-J.; Maillard, F. M.; Dubau, L.; Michalička, J.; Macak, J. M.; Holleitner, A.; Bandarenka, A. S. Top-Down Synthesis of Nanostructured Platinum−Lanthanide Alloy Oxygen Reduction Reaction Catalysts: Pt_xPr/C as an Example. *ACS Appl. Mater. Interfaces* **2019**, *11*, 5129−5135.
(16) Pavesi, D.; van de Poll, R. C. J.; Krasovic, J. L.; Figueiredo, M.; Gruter, G.-J. M.; Koper, M. T. M.; Schouten, K. J. P. Cathodic Disintegration as an Easily Scalable Method for the Production of Sn and Pb-Based Catalysts for CO_2 Reduction. *ACS Sustainable Chem. Eng.* **2020**, *8*, 15603−15610.
(17) Bennett, E.; Monzó, J.; Humphrey, J.; Plana, D.; Walker, M.; McConville, C.; Fermin, D.; Yanson, A. I.; Rodriguez, P. A Synthetic Route for the Effective Preparation of Metal Alloy NPs and Their Use as Active Electrocatalysts. *ACS Catal.* **2016**, *6*, 1533−1539.
(18) Kromer, M. L.; Monzó, J.; Lawrence, M. J.; Kolodziej, A.; Gossage, Z. T.; Simpson, B. H.; Morandi, S.; Yanson, A.; Rodríguez-López, J.; Rodríguez, P. High-Throughput Preparation of Metal Oxide Nanocrystals by Cathodic Corrosion and Their Use as Active Photocatalysts. *Langmuir* **2017**, *33*, 13295−13302.
(19) Duca, M.; Rodriguez, P.; Yanson, A. I.; Koper, M. T. M. Selective Electrocatalysis on Platinum NPs with Preferential (100) Orientation Prepared by Cathodic Corrosion. *Top. Catal.* **2014**, *57*, 255−264.
(20) Katsounaros, I.; Ipsakis, D.; Polatides, C.; Kyriacou, G. Efficient Electrochemical Reduction of Nitrate to Nitrogen on Tin Cathode at Very High Cathodic Potentials. *Electrochim. Acta* **2006**, *52*, 1329−1338.
(21) Li, Y.; Kim, D.; Louisia, S.; Xie, C.; Kong, Q.; Yu, S.; Lin, T.; Aloni, S.; Fakra, S.; Yang, P. Electrochemically Scrambled Nanocrystals are Catalytically Active for CO_2-to-Multicarbons. *Proc. Natl. Acad. Sci. U. S. A.* **2020**, *117*, 9194−9201.
(22) Kim, Y.-G.; Javier, A.; Baricuatro, J. H.; Torelli, D.; Cummins, K. D.; Tsang, C. F.; Hemminger, J. C.; Soriaga, M. P. Surface Reconstruction of Pure-Cu Single-Crystal Electrodes under CO-Reduction Potentials in Alkaline Solutions: A Study by Seriatim ECSTM-DEMS. *J. Electroanal. Chem.* **2016**, *780*, 290−295.
(23) Yang, Y.; Roh, I.; Louisia, S.; Chen, C.; Jin, J.; Yu, S.; Salmeron, M. B.; Wang, C.; Yang, P. *Operando* Resonant Soft X-ray Scattering Studies of Chemical Environment and Interparticle Dynamics of Cu Nanocatalysts for CO_2 Electroreduction. *J. Am. Chem. Soc.* **2022**, *144*, 8927−8931.
(24) Vavra, J.; Shen, T.-H.; Stoian, D.; Tileli, V.; Buonsanti, R. Real-time Monitoring Reveals Dissolution/Redeposition Mechanism in Copper Nanocatalysts during the Initial Stages of the CO_2 Reduction Reaction. *Angew. Chem., Int. Ed.* **2021**, *60*, 1347−1354.
(25) Yang, Y.; et al. Electrocatalysts in Alkaline Media and Alkaline Membrane-Based Energy Technologies. *Chem. Rev.* **2022**, *122*, 6117−6321.
(26) Foster, S. L.; Bakovic, S. I. P.; Duda, R. D.; Maheshwari, S.; Milton, R. D.; Minteer, S. D.; Janik, M. J.; Renner, J. N.; Greenlee, L. F. Catalysts for Nitrogen Reduction to Ammonia. *Nat. Catal.* **2018**, *1*, 490−500.
(27) Cerviño, R. M.; Triaca, W. E.; Arvia, A. J. Electrochemical Preparation and Characteristics of Platinum Electrode Surfaces with Preferred Orientations. *J. Electroanal. Chem.* **1985**, *182*, 51−60.
(28) Gómez, J.; Vázquez, L.; Baró, A. M.; Garcia, N.; Perdriel, C. L.; Triaca, W. E.; Arvia, A. J. Surface Topography of (100)-Type Electro-Faceted Platinum from Scanning Tunnelling Microscopy and Electrochemistry. *Nature* **1986**, *323*, 612−614.
(29) Triaca, W. E.; Arvia, A. J. The Electrochemical Facetting of Metal Surfaces: Preferred Crystallographic Orientation and Roughening Effects in Electrocatalysis. *J. Appl. Electrochem.* **1990**, *20*, 347−356.
(30) Cloud, J. E.; McCann, K.; Perera, K. A. P.; Yang, Y. A Simple Method for Producing Colloidal Palladium Nanocrystals: Alternating Voltage-Induced Electrochemical Synthesis. *Small* **2013**, *9*, 2532−2536.
(31) Cloud, J.; Yoder, T. S.; Harvey, N. K.; Snow, K.; Yang, Y. A Simple and Generic Approach for Synthesizing Colloidal Metal and Metal Oxide Nanocrystals. *Nanoscale* **2013**, *5*, 7368−7378.
(32) Yang, Y.; Xiong, Y.; Zeng, R.; Lu, X.; Krumov, M.; Huang, X.; Xu, W.; Wang, H.; DiSalvo, F. J.; Brock, J. D.; Muller, D. A.; Abruña, H. D. *Operando* Methods in Electrocatalysis. *ACS Catal.* **2021**, *11*, 1136−1178.
(33) Zeng, Z.; Zheng, W.; Zheng, H. Visualization of Colloidal Nanocrystal Formation and Electrode-Electrolyte Interfaces in Liquids using TEM. *Acc. Chem. Res.* **2017**, *50*, 1808−1817.
(34) Williamson, M.; Tromp, R.; Vereecken, P.; Hull, R.; Ross, F. Dynamic Microscopy of Nanoscale Cluster Growth at The Solid−Liquid Interface. *Nat. Mater.* **2003**, *2*, 532−536.
(35) Holtz, M. E.; Yu, Y.; Gunceler, D.; Gao, J.; Sundararaman, R.; Schwarz, K. A.; Arias, T. A.; Abruña, H. D.; Muller, D. A. Nanoscale Imaging of Lithium Ion Distribution during In Situ Operation of Battery Electrode and Electrolyte. *Nano Lett.* **2014**, *14*, 1453−1459.
(36) Karki, K.; Serra-Maia, R.; Stach, E.; Alsem, D. H.; Salmon, N. Realistic bulk electrochemistry in liquid cell microscopy. *Microsc. Microanal.* **2020**, *26*, 1458−1459.
(37) Unocic, R. R.; Sacci, R. L.; Brown, G. M.; Veith, G. M.; Dudney, N. J.; More, K. M.; Walden, F. S., II; Gardiner, D. S.; Damiano, J.; Nackashi, D. P. Quantitative electrochemical measurements using in situ EC-S/TEM devices. *Microsc. Microanal.* **2014**, *20*, 452−461.
(38) Khelfa, A.; Byun, C.; Nelayah, J.; Wang, G.; Ricolleau, C.; Alloyeau, D. Structural Analysis of Single NPs In Liquid by Low-Dose STEM Nanodiffraction. *Micron* **2019**, *116*, 30−35.
(39) Karakulina, O. M.; Demortiere, A.; Dachraoui, W.; Abakumov, A. M.; Hadermann, J. In Situ Electron Diffraction Tomography Using A Liquid-Electrochemical Transmission Electron Microscopy Cell for Crystal Structure Determination of Cathode Materials for Li-Ion Batteries. *Nano Lett.* **2018**, *18*, 6286−6291.
(40) Zuo, J. M.; Tao, J. Scanning Electron Nanodiffraction and Diffraction Imaging. In *Scanning Transmission Electron Microscopy*; Pennycook, S., Nellist, P., Eds.; Springer: New York, 2011.

https://doi.org/10.1021/jacs.2c05989
J. Am. Chem. Soc. XXXX, XXX, XXX−XXX

(41) Ophus, C. Four-Dimensional Scanning Transmission Electron Microscopy (4D-STEM): From Scanning Nanodiffraction to Ptychography and Beyond. *Microsc. Microanal.* **2019**, *25*, 563−582.
(42) Clavilier, J.; Faure, R.; Guinet, G.; Durand, R. Preparation of Monocrystalline Pt Microelectrodes and Electrochemical Study of the Plane Surfaces Cut in Tthe Direction of the {111} and {110} planes. *J. Electroanal. Chem.* **1980**, *107*, 205−209.
(43) Vidal-Iglesias, F. J.; Aran-Ais, R. M.; Solla-Gullon, J.; Herrero, E.; Feliu, J. M. Electrochemical Characterization of Shape-Controlled Pt NPs in Different Supporting Electrolytes. *ACS Catal.* **2011**, *2*, 901−910.
(44) Hersbach, T. J. P.; Ye, C.; Garcia, A. C.; Koper, M. T. M. Tailoring the Electrocatalytic Activity and Selectivity of Pt(111) Through Cathodic Corrosion. *ACS Catal.* **2020**, *10*, 15104−15113.
(45) Arulmozhi, N.; Hersbach, T. J. P.; Koper, M. T. M. Nanoscale Morphological Evolution of Monocrystalline Pt Surfaces During Cathodic Corrosion. *Proc. Natl. Acad. Sci. U. S. A.* **2020**, *117*, 32267−32277.
(46) Jiang, Y.; Chen, Z.; Han, Y.; Deb, P.; Gao, H.; Xie, S.; Purohit, P.; Tate, M. W.; Park, J.; Gruner, S. M.; Elser, V.; Muller, D. A. Electron Ptychography of 2D Materials to Deep Sub-Ångström Resolution. *Nature* **2018**, *559*, 343−349.
(47) German, S. R.; Edwards, M. A.; Ren, R.; White, H. S. Critical Nuclei Size, Rate, and Activation Energy of H_2 Gas Nucleation. *J. Am. Chem. Soc.* **2018**, *140*, 4047−4053.
(48) Holtz, M. E.; Yu, Y.; Gao, J.; Abruña, H. D.; Muller, D. A. *In Situ* Electron Energy-Loss Spectroscopy in Liquids. *Microsc. Microanal.* **2013**, *19*, 1027−1035.
(49) Serra-Maia, R.; Kumar, P.; Meng, A. C.; Foucher, A. C.; Kang, Y.; Karki, K.; Jariwala, D.; Stach, E. A. Nanoscale Chemical and Structural Analysis during In Situ Scanning/Transmission Electron Microscopy in Liquids. *ACS Nano* **2021**, *15*, 10228−10240.
(50) Zhang, J.; Sasaki, K.; Adzic, R. R. Stabilization of Platinum Oxygen-Reduction Electrocatalysts Using Gold Clusters. *Science* **2007**, *315*, 220−222.
(51) Yang, Y.; Xiao, W.; Feng, X.; Xiong, Y.; Gong, M.; Shen, T.; Abruña, H. D.; Wang, D. Golden Palladium Zinc Ordered Intermetallics as Oxygen Reduction Electrocatalysts. *ACS Nano* **2019**, *13*, 5968−5974.
(52) Auffermann, G.; Muller, P.; Bronger, W. Neutron Scattering as a Powerful Tool in Solid State Chemistry. Examples from the Investigations in Crystal Structures and Properties of Metal Hydrogen and Metal Chalcogen Compounds. *Z. Anorg. Allg. Chem.* **2004**, *630*, 2113−2124.
(53) Wang, X.; Andrews, L. Gold is Noble but Gold Hydride Anions are Stable. *Angew. Chem., Int. Ed.* **2003**, *42*, 5201−5206.
(54) Rahm, M.; Hoffmann, R.; Ashcroft, N. W. Ternary Gold Hydrides: Routes to Stable and Potentially Superconducting Compounds. *J. Am. Chem. Soc.* **2017**, *139*, 8740−8751.
(55) Silverwood, I. P.; Rogers, S. M.; Callear, S. K.; Parker, S. F.; Catlow, C. R. A. Evidence for a Surface Gold Hydride on a Nanostructured Gold Catalyst. *Chem. Commun.* **2016**, *52*, 533−536.

https://doi.org/10.1021/jacs.2c05989
J. Am. Chem. Soc. XXXX, XXX, XXX−XXX